Supplementary Material Accompanying:

"Increased hurricane frequency near Florida during Younger Dryas AMOC slowdown" by Toomey, Korty, Donnelly, van Hengstum and Curry.

MODEL CALCULATIONS

We calculated environmental parameters relevant for tropical cyclone genesis and intensification in segments of the coupled TraCE simulation (Liu et al., 2009). These include the YD (12.5 to 12.0 kyrs BP) and EH (10.8 to 10.2 kyrs BP). From monthly-varying data, we calculated the potential intensity (PI), magnitude of the 850 - 200 mb vertical wind shear (VWS), a measure of thermodynamic resistance (c), and a genesis potential index (GPI) used successfully in both contemporary and paleoclimate modeling studies (e.g., Korty et al., 2012).

PI predicts an upper bound on intensity controlled by the release of available potential energy during deep convection; it is a function of both the SST and vertical soundings of temperature and humidity through the troposphere and lower stratosphere. It is also useful as a measure of where TCs can be sustained as regions that cannot support the deep convection have systematically low PI values (Korty et al., 2012). We use an algorithm derived from Bister and Emanuel (2002) to compute potential intensity. First, an average annual cycle was computed for each segment of TraCE examined (e.g., all Januaries in a given segment were averaged together, all Februaries, etc.). Then, PI values at each node in the model domain were averaged from June to November in order to evaluate the Northern Hemisphere seasonal mean. The PI difference between the YD and EH derived from these calculations is shown in Fig. DR3. There is a broad decrease in PI across the tropical Atlantic, but these drops are largest south of 20° N where SSTs fell the most (e.g. Barbados in Fig. 3). In contrast, conditions near Florida remain supportive of Category 5 intensities throughout the YD. Where SSTs fell less than the average for the basin, PI actually rises despite the colder SST (east of southeast U.S. coast). This behavior is consistent with the findings of Vecchi and Soden (2007), who showed that PI is strongly affected by the relative difference between local SSTs and the regional average, not absolute temperature. (Note that difference in PI values in Fig. DR3 are for the June to November mean while the time series in panel (c) of Fig. 3 in the main text show the annual peak value of PI [in whatever month it occurs].)

Humidity in the middle troposphere of the tropics is lower than elsewhere in the column, and if these midlevels are especially dry, a large amount of water will need to be added by convection to saturate the column. The midlevel dryness can be expressed in terms of a moist entropy deficit: the actual temperature and humidity at 600 mb will yield a value of moist entropy (s_m) lower than the value it would have if saturated at the same temperature (s_m^*). Convection in tropical cyclones is fueled primarily by evaporation from the ocean surface, and the strength of this flux is proportional to the air-sea thermodynamic disequilibrium. In terms of entropy, this is the difference between the saturation moist entropy at the surface pressure and SST (s_0^*) and the actual moist entropy of the atmospheric boundary layer (s_b), which is a function of its temperature and humidity. Since the atmospheric boundary layer's temperature is usually in equilibrium with the SST, the deficit is principally related to the fact that the atmosphere is not saturated while the ocean is. The ratio of these two deficits gives a parameter that measures how much water must be added to saturate the dry mid-levels relative to the strength of the flux that provides the moisture; it is defined as:

$$\chi = \frac{s_m^* - s_m}{s_0^* - s_b}$$

and has been shown to be related to the time necessary for TC genesis to occur (Rappin et al., 2010). Interestingly, if relative humidity changes little with climate, the numerator will grow exponentially with temperature, but the denominator grows closer to linearly (e.g., Korty et al., 2017). Thus, colder climates have smaller values of this resistance parameter, which is related to the shorter time needed to saturate a column and form a TC in colder atmospheres. Change in the seasonal (JJASON) mean between the YD and EH TraCE segments is shown in panel (b) of Fig. DR3; the colder YD features lower χ everywhere.

Vertical shear of the 850 and 200 mb winds (VWS) is calculated as the magnitude of the vector difference of the horizontal wind on these two pressure surfaces. Panel (c) of Fig. DR3 shows that shear increases south of 20° N, but north of this latitude shear is little different or weaker during the YD. Combined with the smaller χ across the basin, the thermodynamic effects of wind shear would be reduced north of 20° N (Tang and Emanuel, 2012).

These genesis factors each contribute to the overall environment for TCs. But in cases where one points toward more favorable conditions while another suggests the opposite, it is important to be able to discern their combined and interactive effects. Genesis potential indices have been developed and calibrated against modern observations to assess the combined effects, and we employ the form used in Korty et al. (2012) here. This updates a form developed in Emanuel et al. (2008) but includes the later findings of Tippett et al. (2011) that absolute vorticity η values are important near the equator, but less so at latitudes poleward of ~15° N/S. The genesis potential index is defined as:

$$GPI = \frac{b\,\min(|\eta|, 4\times10^{-5}s^{-1})^3\,\max(PI-35{,}0)^2}{\chi^{\frac{4}{3}}\,(25+VWS)^4}$$

and has units of storms per time per length squared. The coefficient b is a constant selected to normalize the GPI to 90 storms in the 20th century, and we follow the practice of Korty et al. (2012) and set this to a value of 1/1500. We integrate GPI values over each 6-month season and area of 1° latitude-square boxes to ease the interpretation of the numbers in Figure 3.The combination of higher shear and lower PI reduce GPI at low latitudes across the Caribbean and eastern Atlantic, but the smaller changes in shear and PI are outweighed by the drops in χ near Florida. Here GPI is higher during the YD than in the ensuing EH.

DATA-MODEL SST COMPARISON

We compare how the annual mean SST changes between 13 ka and 12 ka in the TraCE simulation with proxy reconstructions of SST changes for the same interval as reported in Renssen et al. (2015; see their DR Table 1, but note our site numbering differs from theirs). We compare six available SST reconstructions from the North Atlantic (Fig. DR4) with the simulated SST change at the model grid point nearest the location of the proxy site in the table below. Sites 1, 2, and 5 are derived from Mg/Ca; sites 3 and 4 from alkenones; and site 6 from diatoms. To compute the model change in SST, we average all SST values over a 50-year period centered on 13 ka and 12 ka and then take their difference. The result lies within the estimated uncertainty of the proxy data at sites 1, 2, 3, and 4; it is 0.6 °C cooler than the lower bound at site 5, and 0.1 °C warmer than the upper bound at Site 6. Both of these lie on the eastern margin of the North Atlantic near Europe (Fig. DR4).

OCEAN HEAT CONTENT

Ocean heat content color map shown in Fig. 1A summarizes NOAA Satellite Ocean Heat Content Suite data (Donahue, 2015; https://data.nodc.noaa.gov/sohcs/). Available daily Ocean Heat Content measurements were averaged over each storm season (June through November) before making a composite for 2013-2015 CE.

ADDITIONAL REFERENCES CITED

Bister, M., and Emanuel, K. A., 2002, Low frequency variability of tropical cyclone potential intensity 1. Interannual to interdecadal variability: Journal of Geophysical Research: Atmospheres, v. 107, no. D24.

Blott, S. J., and Pye, K., 2006, Particle size distribution analysis of sand-sized particles by laser diffraction: an experimental investigation of instrument sensitivity and the effects of particle shape: Sedimentology, v. 53, no. 3, p. 671-685.

Donahue, D., and U.S. Department of Commerce; National Oceanic and Atmospheric Administration; National Environmental Satellite Data and Information Service, 2015, Satellite Ocean Heat Content Suite from 2013–06–01 to 2015–11–31 (NCEI Accession 0139511), Version 1.1: Asheville, North Carolina, NOAA National Centers for Environmental Information, Dataset. May 2016.

Emanuel, K., Sundararajan, R., and Williams, J., 2008, Hurricanes and global warming: Results from downscaling IPCC AR4 simulations: Bulletin of the American Meteorological Society, v. 89, no. 3, p. 347-367.

Koc Karpuz, N., and Jansen, E., 1992, A high-resolution diatom record of the last deglaciation from the SE Norwegian Sea: documentation of rapid climate changes: Paleoceangraphy, v. 7, p. 499-502.

Korty, R. L., Camargo, S. J., and Galewsky, J., 2012, Tropical cyclone genesis factors in simulations of the Last Glacial Maximum: Journal of Climate, v. 25, no. 12, p. 4348-4365.

Korty, R. L., Emanuel, K. A., Huber, M., and Zamora, R. A., 2017, Tropical Cyclones Downscaled from Simulations with Very High Carbon Dioxide Levels: Journal of Climate, v. 30, no. 2, p. 649-667.

Liu, Z., Otto-Bliesner, B., He, F., Brady, E., Tomas, R., Clark, P., Carlson, A., Lynch-Stieglitz, J., Curry, W., and Brook, E., 2009, Transient simulation of last deglaciation with a new mechanism for Bølling-Allerød warming: Science, v. 325, no. 5938, p. 310-314.

Lynch-Stieglitz, J., Schmidt, M. W., and Curry, W. B., 2011, Evidence from the Florida Straits for Younger Dryas ocean circulation changes: Paleoceanography, v. 26, no. 1, p. PA1205.

Pailler, D., and Bard, E., 2002, High frequency palaeoceanographic changes during the past 140 000 yr recorded by the organic matter in sediments of the Iberian Margin: Palaeogeogr. Palaeoclim. Palaeoecol., v. 181, p. 431-452.

Peck, V.L., Hall, I.R., Zahn, R., and Elderfield, H., 2008, Millennial-scale surface and subsurface paleothermometry from the northeast Atlantic, 55-8 ka BP: Paleoceanography, v. 23, doi:10.1029/2008PA001631.

Rappin, E. D., Nolan, D. S., and Emanuel, K. A., 2010, Thermodynamic control of tropical cyclogenesis in environments of radiative-convective equilibrium with shear: Quarterly Journal of the Royal Meteorological Society, v. 136, no. 653, p. 1954-1971.

Renssen, H., Aurelien, J., Goosse, H., Mathiot, P., Heiri, O., Roche, D.M., Nisancioglu, K.H., and Valdes, P.J., 2015, Multiple causes of the Younger Dryas cold period: Nature Geoscience, v. 8, p. 946-949, doi:10.1038/ngeo2557.

Rodrigues, T., Grimalt, J.O., Abrantes, F., Naughton, F., and Flores, J.A., 2010: The last glacial-interglacial transition (LGIT) in the western mid-latitudes of the North Atlantic: Abrupt sea surface temperature change and sea level implications: Quaternary Science Review, v. 29, p. 1853-1862.

Sachs, J. P., 2007, Cooling of Northwest Atlantic slope waters during the Holocene: Geophysical Research Letters, v. 34, L03609, doi:10.1029/2006GL028495.

Tang, B., and Emanuel, K., 2012, A ventilation index for tropical cyclones: Bulletin of the American Meteorological Society, v. 93, no. 12, p. 1901-1912.

Tippett, M. K., Camargo, S. J., and Sobel, A. H., 2011, A Poisson regression index for tropical cyclone genesis and the role of large-scale vorticity in genesis: Journal of Climate, v. 24, no. 9, p. 2335-2357.

Vecchi, G. A., and Soden, B. J., 2007, Effect of remote sea surface temperature change on tropical cyclone potential intensity: Nature, v. 450, no. 7172, p. 1066-1070.

Weltje, G. J., and Tjallingii, R., 2008, Calibration of XRF core scanners for quantitative geochemical logging of sediment cores: theory and application: Earth and Planetary Science Letters, v. 274, no. 3, p. 423-438.

Williams, C., et al., 2010, Deglacial abrupt climate change in the Atlantic Warm Pool: A Gulf of Mexico perspective: Paleoceanography, v. 25, PA4221, doi:10.1029/2010PA001928.

ADDITIONAL FIGURES

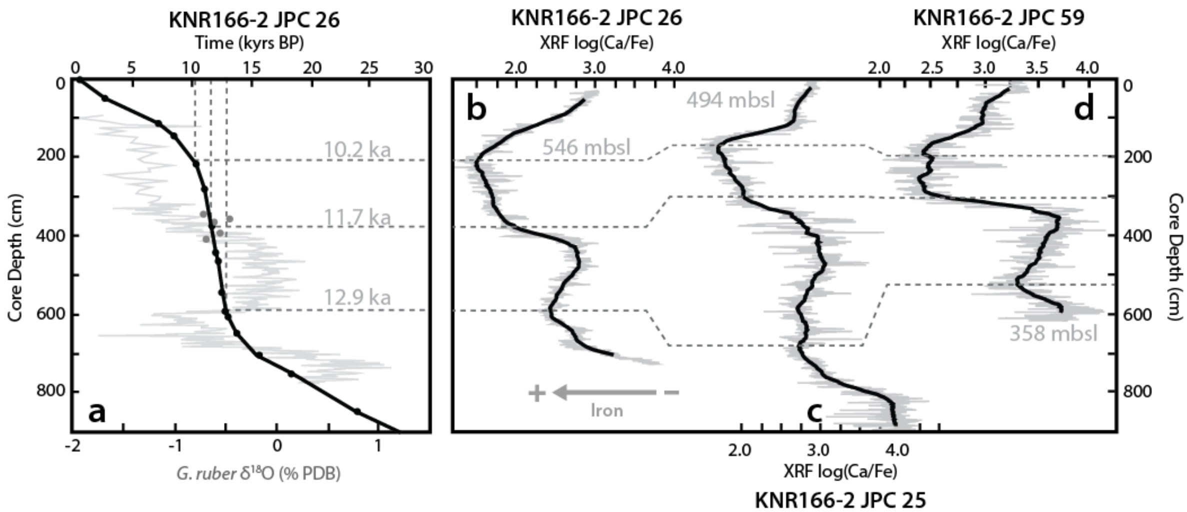

Figure DR1. Chronology and graphical correlation of cores. **(a)** Radiocarbon dates (circles) and chronology (black line) and *G. ruber* $\delta^{18}O$ for KNR166-2 JPC26 (Lynch-Stieglitz et al., 2011). XRF ln(Ca/Fe) relative abundance measurements for Florida Straits offbank transect (Figure 1). Log-normal ratios of XRF elemental abundances were used to account for possible downcore changes in grain-size and water content (Weltje and Tjallingii, 2008). **(b)** KNR166-2 JPC 26 (24.3267 °N, 83.2524 °W), **(c)** KNR166-2 JPC 25 (24.3432 °N, 83.2488 °W), and **(c)** KNR166-2 JPC 59 (24.4175 °N, 83.3682 °W). Black line gives 50 cm moving average filtered XRF data. Linear sedimentation was assumed between tie points (grey dashed lines). Core-top of JPC26 not included due to possible disturbance. Some section edges (~few cm) not included due to possible disturbance and/or changes in water content likely to have affected XRF values. Measurement depths were corrected for desiccation during core storage.

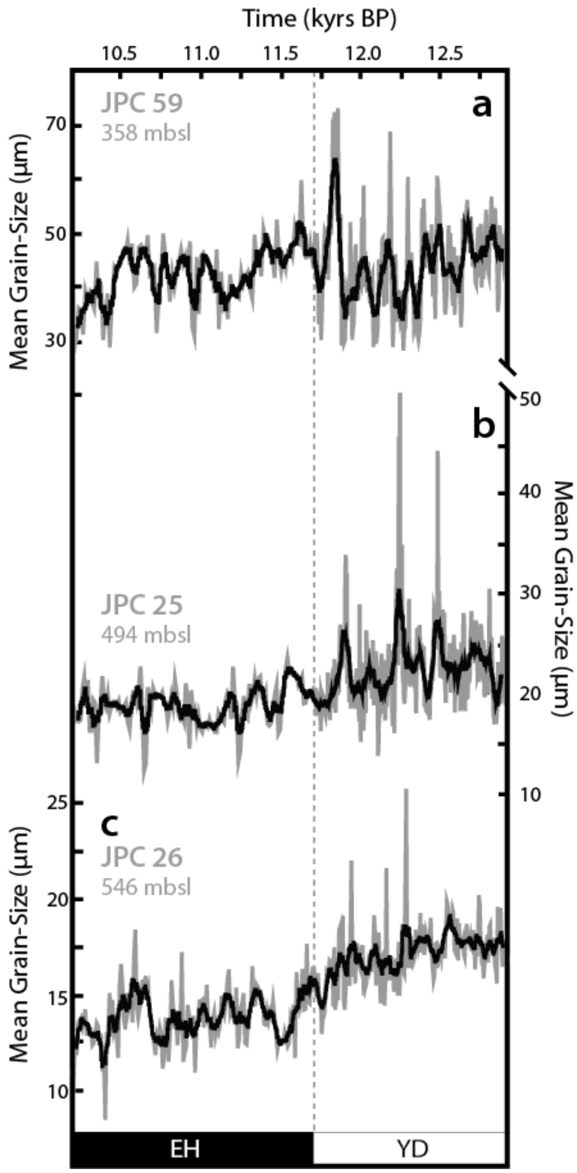

Figure DR2: Grain-size records from Florida Straits offbank core transect: **(a)** KNR166-2 JPC59, **(b)** KNR166-2 JPC25 and **(c)** KNR166-2 JPC26. We note that the magnitudes of the largest grain-size peaks above background are much smaller in JPC26 (~5 − 10 μm) than in JPC25/59 (~15 − 30 μm) and are taken as suggestive given previous work demonstrating laser particle size sensitivity to grain shape (up to 21 % relative to the wet-sieving) (Blott and Pye, 2006). Black line shows 50-yr moving average filtered grain-size for each core. All measurement depths were corrected for core desiccation prior to interpolating age models.

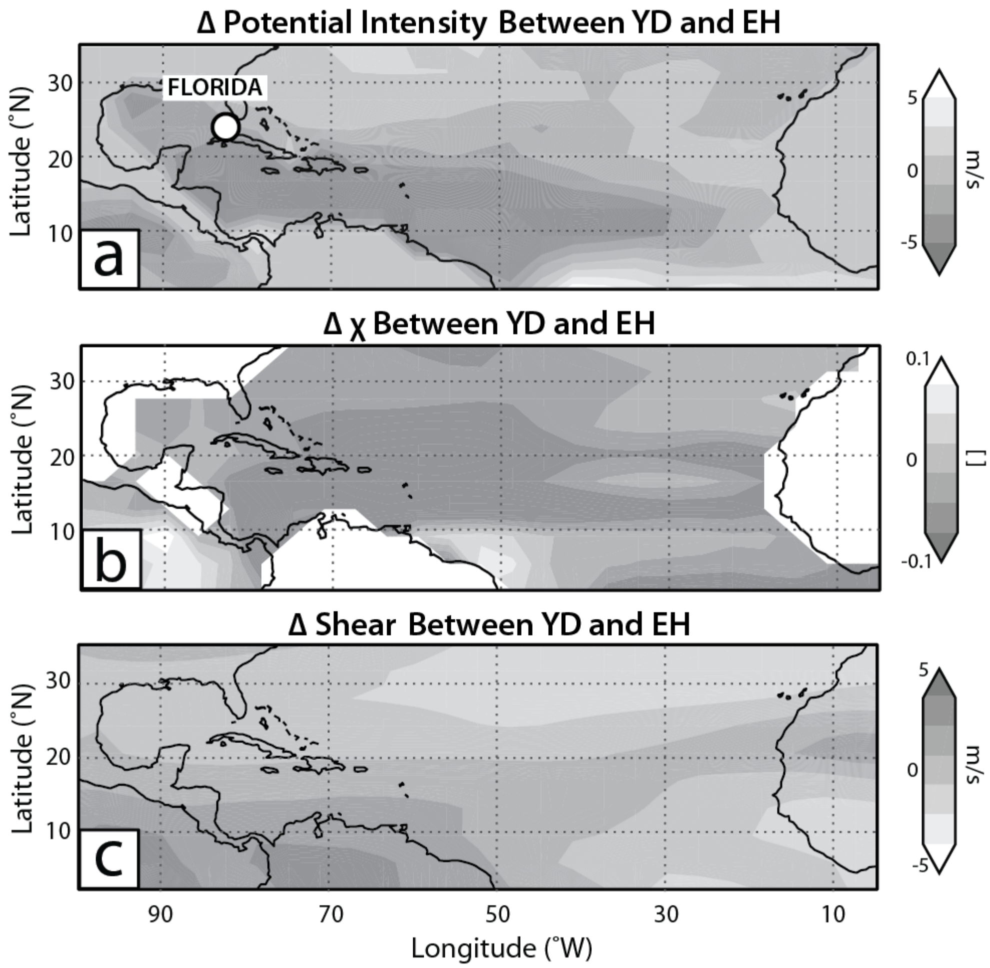

Figure DR3: TC variables computed from TraCE output showing YD to EH difference in: **(a)** potential intensity, **(b)** chi and **(c)** shear.

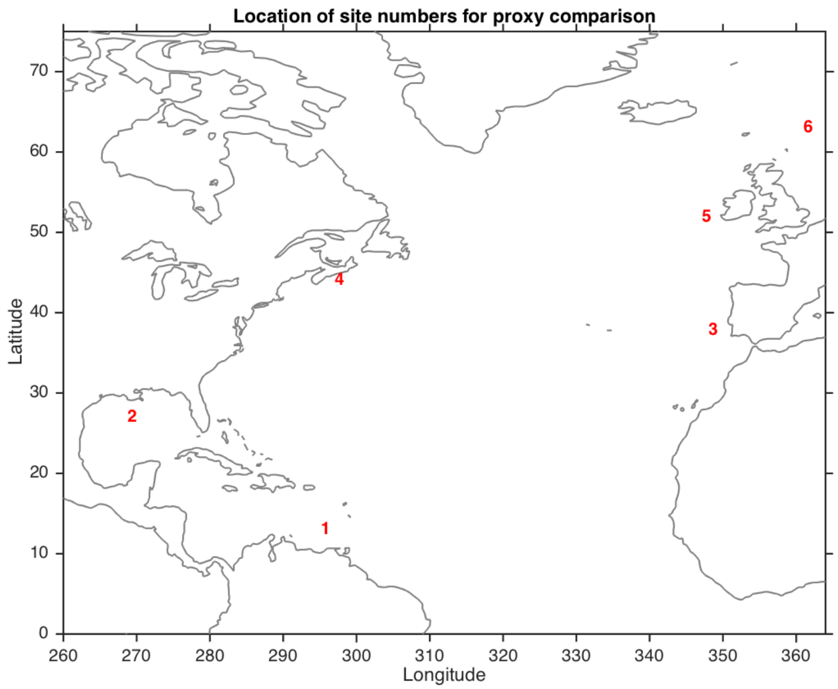

Fig. DR4: Location of SST proxy reconstruction sites for comparison to model derived data.

Table DR1

Site No.	Location	Latitude	Longitude	Proxy 12ka-13ka ΔSST (annual mean; °C)	Model 12ka-13ka ΔSST (annual mean; °C)	Proxy source
1	PL07-39PC, Cariaco Basin	13.0 N	64.9 W	-2.9 ± 1.4	-1.6	Lea et al. (2006)
2	MD02-2550, Orca Basin	26.9 N	91.3 W	-1.9 ± 1.4	-0.5	Williams et al. (2010)
3	MD952042, Iberian Margin; D13882, Iberian Margin	37.8 N	12.0 W	-1.5 ± 1.0	-2.5	Pailler and Bard (2002); Rodrigues et al. (2010)
4	OCE326-GGC30, NW Atlantic Slope	44.0 N	63.0 W	-1.0 ± 1.0	-0.1	Sachs (2007)
5	MD01-2461, Northeast Atlantic	51.8 N	12.9 W	-2.0 ± 1.4	-4.0	Peck et al. (2008)
6	HM79-6/4, Norwegian Sea	63.0 N	1.0 E	-5.2 ± 2.0	-3.1	Koc Karpuz and Jansen (1992)

ADDITIONAL DATA

Bulk mean grain-size data for JPC25 is included as Data Repository item.

Additional data available from Michael Toomey (mrt02008@gmail.com).